

Hundness and band renormalization in the kagome antiferromagnets Mn_3X

Yingying Cao,^{1,2} Yuanji Xu,³ and Yi-feng Yang^{1,2,4,*}

¹*Beijing National Laboratory for Condensed Matter Physics and Institute of Physics,
Chinese Academy of Sciences, Beijing 100190, China*

²*School of Physical Sciences, University of Chinese Academy of Sciences, Beijing 100049, China*

³*Institute for Applied Physics, University of Science and Technology Beijing, Beijing 100083, China*

⁴*Songshan Lake Materials Laboratory, Dongguan, Guangdong 523808, China*

(Dated: May 3, 2024)

The interplay of topological band structures and electronic correlations may lead to novel exotic quantum phenomena with potential applications. First-principles calculations are critical for guiding the experimental discoveries and interpretations, but often fail if electronic correlations cannot be properly treated. Here we show that this issue occurs also in the antiferromagnetic kagome lattice Mn_3X ($X = \text{Sn}, \text{Ge}$), which exhibit a large anomalous Hall effect due to topological band structures with Weyl nodes near the Fermi energy. Our systematic investigations reveal a crucial role of the Hund's rule coupling on three key aspects of their magnetic, electronic, and topological properties: (1) the establishment of noncollinear antiferromagnetic orders, (2) the weakly renormalized bands in excellent agreement with ARPES, and (3) a sensitive tuning of the Weyl nodes beyond previous expectations. Our work provides a basis for understanding the topological properties of Mn_3X and challenges previous experimental interpretations based on incorrect band structures.

Topological quantum materials have attracted intensive interest for their importance on both fundamental physics and potential applications. Increasing attentions have recently focused on correlated topological materials, in which exotic many-body phenomena may emerge due to the interplay of nontrivial topology and electronic correlations^{1,2}. One notable example is Mn_3Sn , which adopts a kagome bilayer structure and exhibits a noncollinear triangular antiferromagnetic (AFM) order in the kagome plane below 430 K^{3,4}. This compound has a considerable spin-orbit coupling (SOC) that breaks the effective time reversal symmetry and may cause nonzero Berry curvatures and sizable anomalous Hall conductivities without external magnetic field⁵. A large anomalous Hall effect (AHE) has indeed been observed at room temperature despite of the vanishingly small net magnetization⁴. Resistivity and thermal conductivity measurements reported an anomalous Lorenz number and excluded its origin from inelastic scattering⁶. A large magneto-optical Kerr effect (MOKE) was also observed, implying the presence of analogous symmetry requirement for the AHE⁷. Hence, Mn_3Sn has been established to be the first AFM material with intrinsic AHE.

First-principles calculations of electronic band structures played a key role in guiding the above experimental discoveries and interpretations. Density functional theory (DFT) studies of Mn_3Sn predicted the existence of Weyl points near the Fermi energy⁸⁻¹⁰, which are singular points of Berry curvatures (magnetic monopoles in momentum space)^{11,12} and may give a large contribution to the AHE. Comparison with the angle-resolved photoemission spectroscopy (ARPES) experiment¹³ seems to support the predicted DFT band structures, but requires

a very large band renormalization factor of about 5, suggesting significant electronic correlations. However, the effects of electronic correlations typically cannot be captured by DFT. In addition, the Hund's rule coupling is also not well treated but has been shown to be important for the partially filled $3d$ shell^{14,15}, especially in Mn-based compounds¹⁶. This raises the concern on the reliability of the DFT-predicted band structures, which has not been paid much attention in previous studies.

Mn_3Ge is an isostructural compound with the same noncollinear triangular AFM order and a small residual in-plane magnetic moment below 380 K¹⁷. It exhibits similar giant AHE, anomalous Nernst effect, and MOKE¹⁸⁻²⁰, suggesting similar electronic structure compared to Mn_3Sn . However, comparison between DFT calculations with ARPES measurements yields a small renormalization factor of 1.18, in sharp contrast to that of Mn_3Sn ²¹. This large divergence between two similar compounds also calls for reinvestigation of their correlated electronic structures. This issue becomes particularly important considering that DFT predictions of the Weyl points have been widely adopted in experimental interpretations, although their presence has not been visualized in ARPES. Recent DFT+U calculations have even claimed possible topological phase transition with the onsite Coulomb interaction²².

In this work, we show that the Hund's rule coupling is critical in resolving the above controversy. We performed systematic correlated electronic structure calculations by combining DFT²³ and the dynamical mean-field theory (DMFT)²⁴⁻²⁹, taking into account the onsite Hubbard repulsion, the Hund's rule coupling, and the SOC. Detailed comparison with ARPES data uncovers a primary role of the Hund's rule coupling on some key aspects of the magnetic, electronic, and topological properties of both Mn_3Sn and Mn_3Ge . By determining the Mn-ionic configurations, it helps to establish their

*yifeng@iphy.ac.cn

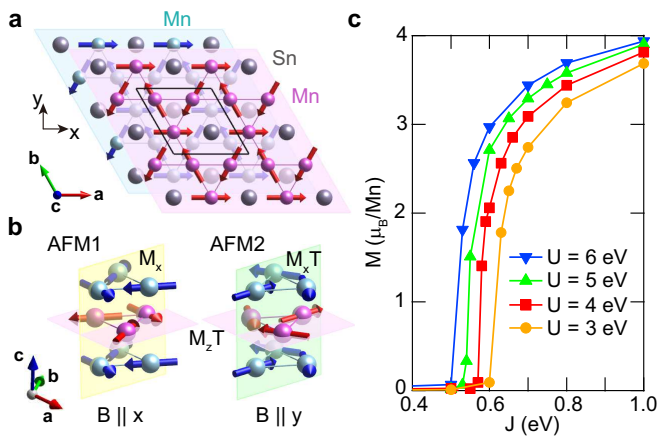


FIG. 1: **Crystal and magnetic properties.** **a** Illustration of the crystal structure of Mn_3Sn with AFM1 magnetic configuration showing inverse symmetry between two adjacent Mn_3Sn layers³⁰; **b** Symmetry of the triangular antiferromagnetic order for two spin configurations, AFM1 and AFM2, depending on the applied magnetic field $B \parallel x$ and $B \parallel y$, respectively. Three mirror planes are shown for $M_z T$ (magenta), M_x (yellow), and $M_x T$ (green), where M_x and M_z are mirror operations and T is the time reversal operation. **c** The spin moment of a single Mn-ion in Mn_3Sn for different choices of U and J calculated using DFT+DMFT at 300 K.

spin polarization and hence the AFM order and yield correct electronic band structures in excellent agreement with ARPES data in many fine details. We obtain a much smaller renormalization factor ($Z^{-1} \approx 1.6$) of Mn_3Sn than previously expected from DFT-ARPES comparison. The Weyl nodes are found to depend sensitively on the Hund's rule coupling and may evolve into line nodes with varying parameters. A similar renormalization is also obtained in Mn_3Ge by comparing our calculations and latest ARPES measurements. These reveal the potential importance of Hund physics for understanding their exotic topological properties.

Results

Structural and magnetic analyses. Mn_3X adopt a hexagonal structure with the space group $P6_3/mmc$. The lattice constants are $a = 5.67 \text{ \AA}$ and $c = 4.53 \text{ \AA}$ for Mn_3Sn and $a = 5.39 \text{ \AA}$ and $c = 4.35 \text{ \AA}$ for Mn_3Ge ^{31,32}. The Mn-ions form a kagome lattice with mixed triangles and hexagons in the ab -plane, and the Sn(Ge)-ions are located at the center of the hexagons. As shown in Fig. 1a for Mn_3Sn , the adjacent layers stack along the c -axis with an offset. Below the Néel temperature, a noncollinear AFM state is formed with the Mn moments aligned in the ab -plane and forming an inverse triangular spin structure^{3,33}. As the temperature decreases below 200 K, a helical or incommensurate spin structure may appear in Mn_3Sn depending sensitively on the samples and suppress the triangular AFM until a spin glass is formed below about 50 K³⁴. For simplicity, we will only

consider the inverse triangular AFM phase, in which the inverse symmetry is preserved to transform the two kagome layers to each other. As illustrated in Fig. 1b, there exist two quenched triangular spin configurations, AFM1 and AFM2. While Mn_3Ge is reported to adopt AFM2 order as the ground state³³, the AFM configuration of Mn_3Sn switches between two orders depending on the direction of the applied magnetic field³⁵. The coplanar AFM1 order has two additional symmetries: the mirror symmetry M_x and the combined symmetry $M_z T$. The mirror reflection reverses the components of Berry curvatures parallel to the mirror plane and the time reversal symmetry (T) reverses the Berry curvatures along all directions. Since the Berry curvatures are not affected by the inverse symmetry, the Hall conductivity given by their integration over the Brillouin zone is only nonzero along x direction. Similarly, the AFM2 has $M_z T$ and $M_x T$ symmetries, with the only nonzero component of Hall conductivity along y direction. In real materials, M_x and $M_x T$ can be broken due to a tiny net moment in ab -plane¹³, causing nonzero anomalous Hall conductivity in both x and y directions. This was ignored in previous first-principles calculations^{10,13}. Our DFT+DMFT results in Supplementary Fig. S3 confirm that it is indeed a small perturbation to the electronic band structures. We will therefore focus on the ideal inverse triangular antiferromagnetic orders here.

Effects of the Hund's rule coupling in Mn_3Sn . We only consider AFM1 for Mn_3Sn , whose electronic band structures have been measured by ARPES¹³. Figure 1c plots the calculated Mn spin moment as a function of the Hubbard U and the Hund's rule coupling J . Such a value of the Hund's rule coupling is reasonable for Mn-ions and has been widely used in the literature^{36,37}. The calculations were carried out using DFT+DMFT at 300 K below $T_N = 430 \text{ K}$. For each value of U , the AFM order can only be stabilized for sufficiently large J . The critical J_c lies roughly between 0.5 and 0.6 eV and varies slightly when U increases from 3 to 6 eV. Its increase with decreasing U indicates their compensating role for local spin polarization. Without the Hund's rule coupling, the moment no longer exists and the triangular AFM order cannot be formed regardless of the value of U , at least within our calculated parameter range. By contrast, the size of the moment grows quickly as $J > J_c$, implying its sensitive dependence on the Hund's rule coupling. Thus, the Hund's rule coupling plays a key role in establishing the AFM order in Mn_3Sn , which was not well noticed in previous studies³⁸.

To understand what happens, we plot in Figs. 2a and 2b the projection of the calculated DMFT states on the ionic configurations (N, S_z) of the Mn-3d orbitals for a fixed $U = 6 \text{ eV}$ and different values of J ³⁹. Here N is the occupation number of electrons on Mn-3d orbitals and S_z is the local z -component of the total spin. For $J = 0$ shown in Fig. 2a, we find strong fluctuations among the three valence states $N = 4, 5, 6$ indicated by the

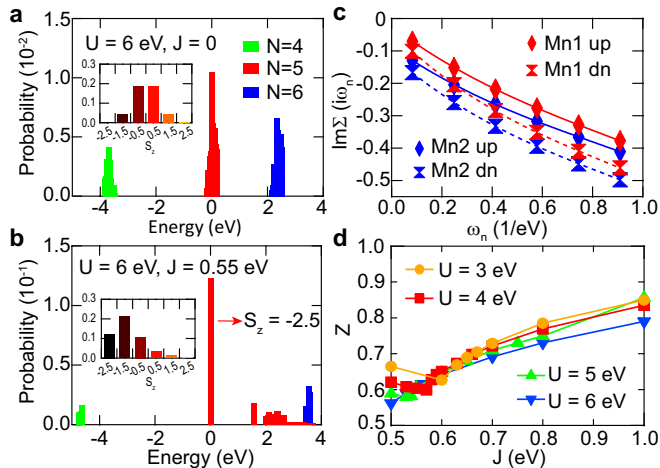


FIG. 2: **Effect of the Hund's rule coupling on the Mn-ionic states and band renormalization in Mn_3Sn .** **a, b** Probabilistic distribution of the DMFT state on different Mn-ionic configurations with the electron occupancy $N = 4, 5, 6$ with ($J = 0.55 \text{ eV}$) and without the Hund's rule coupling at $U = 6 \text{ eV}$. The horizontal axis denotes their respective energy difference with respect to the configuration of largest probability. The insets show the distribution of $N = 5$ state on the local z -component of the total spin, S_z . **c** Illustration of the fourth-order polynomial fitting (solid and dashed lines) to the imaginary part of the orbital-averaged self-energy as a function of the Matsubara frequency for $U = 6 \text{ eV}$ and $J = 0.55 \text{ eV}$. **d** The renormalization factor Z estimated from the DFT+DMFT self-energies with varying U and J .

similar probabilities of DMFT state on these configurations. Meanwhile, the spin also distributes equally along opposite directions, with the highest probability in the $S_z = \pm 0.5$ low spin states. The system is in a nonmagnetic phase despite of the large Hubbard $U = 6 \text{ eV}$. By contrast, once the Hund's rule coupling $J = 0.55 \text{ eV}$ is switched on as shown in Fig. 2b, the $N = 5$, $S_z = -2.5$ state becomes dominant and the Mn-spins become polarized, with most of the weight on negative S_z albeit fluctuating strongly among $S_z = -2.5, -1.5$, and -0.5 . The total spin moment is about $2.6 \mu_B/\text{Mn}$, smaller than the DFT prediction of $3.3 \mu_B$. We will show that this difference is crucial for yielding a spectral function consistent with ARPES measurement¹³. From experiments^{3,35}, the estimated value of magnetic moment varies from 1.78 to $3.0 \mu_B$ depending on the detection technologies, temperature and samples, whose implications await a better understanding.

The strength of electronic correlations may be seen straightforwardly from the band renormalization. Figure 2c plots the orbital-averaged self-energies $\Sigma(i\omega)$ in Matsubara frequency for different spin directions and inequivalent Mn-ions. We find that they behave similarly on two inequivalent ions, possibly due to their similar crystal field environments. The solid and dashed lines give the fourth-order polynomial fitting¹⁵,

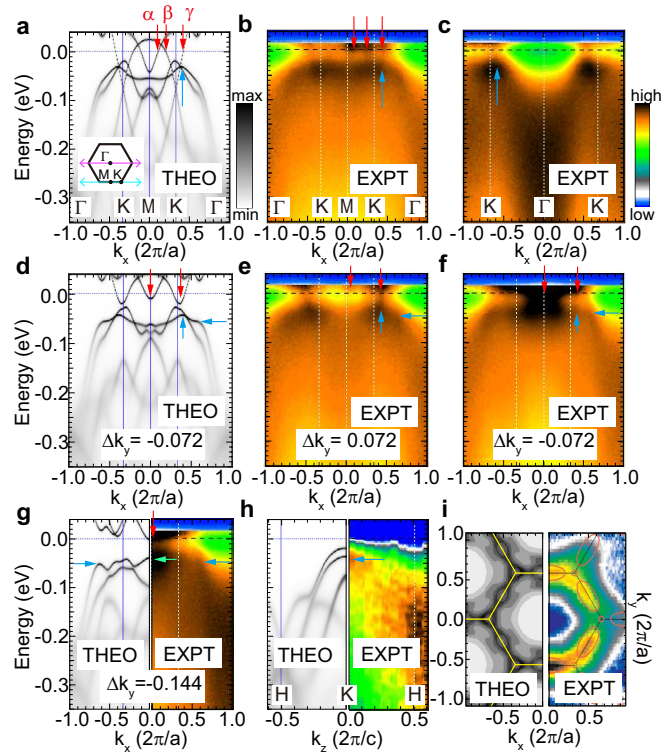


FIG. 3: **Comparison of ARPES¹³ and DFT+DMFT band structures in Mn_3Sn .** Intensity map of the theoretical and experimental spectral functions along: **a, b** the high symmetry Γ -K-M-K- Γ line (cyan arrows in the inset of **a**); **c** the high symmetry M-K- Γ -K-M line (magenta arrows in the inset of **a**); **d-f** the k_x direction with $|\Delta k_y| = 0.072 (2\pi/a)$ slightly off the Γ -K-M-K- Γ path; **g** the k_x direction with $\Delta k_y = -0.144 (2\pi/a)$ from Γ -K-M-K- Γ ; **h** the high symmetry H-K-H line. The arrows of different colors highlight some characteristic features of excellent agreement. **i** Comparison of the theoretical and experimental Fermi surface mapping in the $k_z = 0$ plane. To mimic the low resolution of the ARPES data, we have intentionally chosen the DFT+DMFT results at 300 K . The calculated Fermi surfaces are qualitative the same at 60 K . The yellow line in the left one indicates the hexagonal Brillouin zone. The red curves show the DFT-predicted Fermi surfaces reproduced from Ref.¹³.

which we use to estimate the renormalization factor $Z^{-1} = 1 - \partial \text{Im}\Sigma(i\omega)/\partial \omega|_{\omega \rightarrow 0^+}$. For clarity, we take the average over all Mn-3d orbitals in the unit cell and plot the derived Z as a function of U and J in Fig. 2d. Interestingly, Z increases gradually with increasing J in the AFM phase for $J > J_c$, but behaves oppositely in the paramagnetic phase. This trend may come from the enhanced spin fluctuations near the critical point. At J_c , we obtain a maximum band renormalization Z^{-1} , which is, however, less than 1.8 and hence three times smaller than previous estimate from the comparison between DFT and ARPES in Mn_3Sn ¹³.

Comparison with ARPES on Mn_3Sn . The much

smaller renormalization factor questions the validity concerning the interpretation of ARPES data using the artificially renormalized DFT band structures. In fact, as shown in Supplementary Fig. S1, the renormalized DFT bands fail to conform to experimental observations in many aspects on a qualitative level. Surprisingly, we find that DFT+DMFT can actually give an excellent agreement with the ARPES data for reasonable parameters. Figure 3 shows the intensity map of the spectral function along different line cuts in the Brillouin zone. The ARPES data were reproduced from Ref. 13 and the calculations were performed for $U = 6$ eV and $J = 0.55$ eV at $T = 60$ K. As compared in Figs. 3a-3c, DFT+DMFT successfully captures several major features of the ARPES along the high symmetry path M-K- Γ , where three bands labeled as α, β , and γ cross the Fermi energy (red arrows) and a flat band appears around M at about -0.05 eV. The latter exhibits a peak near the K point (blue arrows), then bends down, and reaches about -0.3 eV at Γ . By contrast, DFT gives a flat band close to the M point at about -0.25 eV (Supplementary Fig. S1), which is far away from the Fermi energy and hence has to be renormalized by a factor of 5 to explain the ARPES observation. But the large artificial renormalization induces a lot of spectral weights between -3 and -1 eV near K-M (Supplementary Fig. S1), which are not present in experiment¹³.

Away from the high symmetry path by $\Delta k_y = -0.072$, two bands (red arrows) were observed to cross the Fermi energy along k_x in ARPES, as plotted in Figs. 3e and 3f. This feature is well captured in DFT+DMFT as marked by the arrows in Fig. 3d. The numerical results provide a better view on the band evolution with k_y . Further away from the high symmetry path, the conduction bands gradually move upwards and the number of bands crossing the Fermi energy decreases. For $\Delta k_y = -0.144$ in Fig. 3g, only the α band (red arrow) crosses the Fermi energy. The bands that intersect around K start to open a gap, display a shoulder (blue arrows), and bulge upward at $k_x = 0$ (green arrow). All features are in good consistency with experiment.

The dispersion along another high symmetry line K-H is also compared in Fig. 3h. The quantitative agreement with ARPES again supports our DFT+DMFT calculations, while in DFT, the renormalization would cause an almost flat band along K-H as shown in Supplementary Fig. S1, which is missing in ARPES. Figure 3i compares the projected Fermi surfaces on $k_z = 0$ plane. We find a better agreement between ARPES and DFT+DMFT. In particular, both have larger Fermi surfaces around some K points than those of DFT (red lines).

These band features depend sensitively on the Hund's rule coupling as discussed in detail in Supplementary Sec. B and Fig. S2. For a slightly larger $J = 0.6$ eV, the flat band around M moves further away from the Fermi energy to about -0.1 eV, and many other features also deviate from ARPES observations. This highlights the importance of the Hund's rule coupling via tuning the

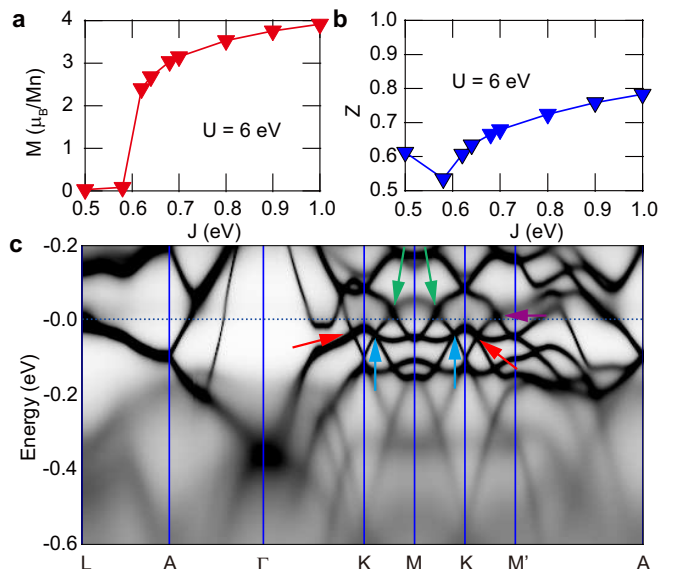


FIG. 4: **Electronic structures of Mn_3Ge .** **a** The spin moment of Mn-ions in Mn_3Ge as a function of the Hund's rule coupling J calculated using DFT+DMFT for fixed $U = 6$ eV at 300 K. **b** The renormalization factor Z extracted from the DFT+DMFT self-energies with varying J at $U = 6$ eV. **c** The spectral function along the high symmetry line L-A- Γ -K-M-K-M'-A at $J = 0.62$ eV, $U = 6$ eV, $T = 300$ K.

spin states of the Mn-ions, and explains why DFT fails to yield the correct band structures even with a large renormalization factor.

Correlation effects in Mn_3Ge . To further support our calculations, we also investigated the effects of the Hund's rule coupling in Mn_3Ge . Figure 4a shows the variation of the Mn spin moment as a function of J for a fixed $U = 6$ eV from DFT+DMFT calculations for the triangular antiferromagnetic configuration. Again, we find a critical $J_c \approx 0.58$ eV, above which the spin moment first grows rapidly and then gradually saturates to about $4 \mu_B/\text{Mn}$ at $J = 1$ eV. The slightly larger J_c suggests that the Mn ions are harder to be polarized in Mn_3Ge than in Mn_3Sn , consistent with the smaller moment length estimated by spherical neutron polarimetry^{3,33}. The band renormalization factor Z is shown in Fig. 4b and varies only gradually from 0.5 to 0.8, indicating weak electronic correlations in Mn_3Ge . At $J = 0.62$ eV close to the observed spin moment $2.65 \mu_B/\text{Mn}$ ³³, our DFT+DMFT calculations also result in a small $Z^{-1} \approx 1.6$.

For comparison with ARPES, we plot in Fig. 4c the DFT+DMFT spectral function along a high symmetry path. Flat bands are clearly seen around -0.05 eV along the K-M path and bend steeply downwards halfway along K- Γ . Around Γ , there are additional dispersive bands bending down towards K and A below -0.38 eV. All these features are in good consistency with latest ARPES measurements²¹ without any artificial renor-

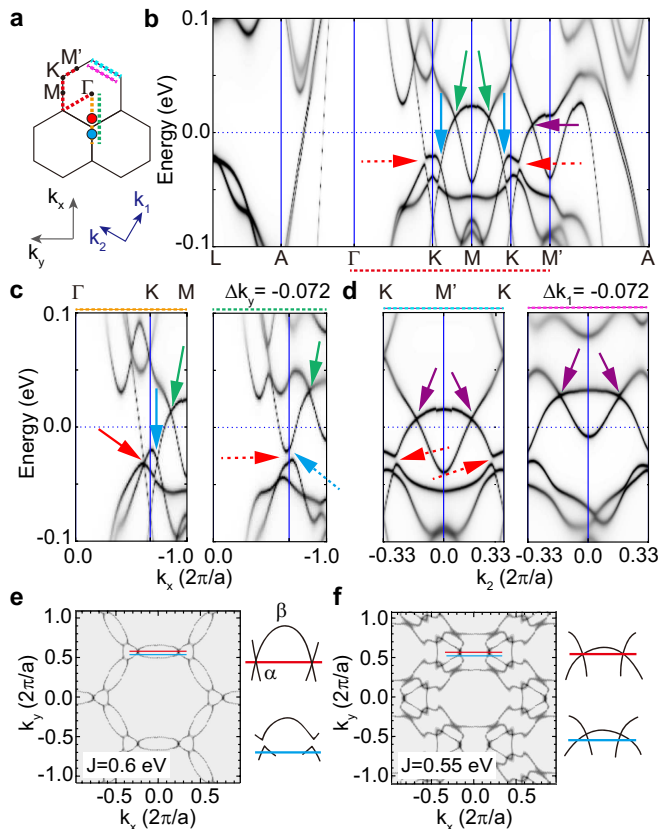


FIG. 5: **Effect of the Hund's rule coupling on the Weyl points in Mn_3Sn .** **a** Illustration of the selected k -paths marked by dashed lines of different colors on the $k_z = 0$ plane of the Brillouin zone. **b** The spectral function along the high symmetry line L-A- Γ -K-M-K-M'-A, where Γ -K-M-K-M' is denoted by the red dashed line in **a** and the arrows mark the band crossings or gaps. **c** Comparison of the spectral functions along Γ -K-M (orange dashed line) and the line shifted by $\Delta k_y = -0.072 (2\pi/a)$ (green dashed line). Note that the orange Γ -K-M line is different from the red one because of the lack of six-fold rotational symmetry. **d** Comparison of the spectral function along K-M'-K (cyan dashed line) and the line shifted by $\Delta k_1 = -0.072 (2\pi/a)$ (pink dashed line). **e, f** The band maps on the $k_z = 0$ plane at $E = 9$ meV for $J = 0.6$ eV and $E = 50$ meV for $J = 0.55$ eV, illustrating the evolution of the band crossings with the Hund's rule coupling.

malization. The overall consistency for both Mn_3Ge and Mn_3Sn validates our systematic DFT+DMFT calculations for these two isostructural compounds.

Tuning the Weyl points. Weyl points in Mn_3X were predicted to be present near the Fermi energy in DFT and may contribute significantly to the AHE⁸⁻¹⁰. Their presence in Mn_3Sn is supported by the observation of a large anomalous Nernst effect beyond that in ferromagnetic metals⁴⁰ and the chiral anomaly in magnetotransport⁴¹. To see if they might be affected, we study in detail the DFT+DMFT band structures for $U = 6$ eV and

$J = 0.55$ eV along different paths in the Brillouin zone marked by dashed lines of different colors in Fig. 5a. Figure 5b shows several crossing points of non-degenerate linear bands along the high symmetry path L-A- Γ -K-M-K-M'-A (red dashed line): two at about -30 meV between K and M marked by blue arrows, two at about 13 meV marked by green arrows, and one at about 8 meV marked by the purple arrow. These crossing points are candidate Weyl points to be examined in more details. In addition, there are two small gaps (red arrows) near K along the Γ -K and K-M' paths. We first focus on the dispersion near K and M and take the path along the k_x direction. In Fig. 5c, it is seen that among all three band crossings along Γ -K-M, only those around the K point (red and blue arrows) become gapped when the path is moved slightly by $\Delta k_y = -0.072$, while the one around M (green arrows) remains unchanged. These indicate that those marked by red and blue arrows are Weyl points, while the one marked by green arrow is a part of line nodes. Note that the Γ -K path (orange dashed line) in Fig. 5c is different from the Γ -K path (red dashed line) in Fig. 5b. Along the K-M'-K path in Fig. 5d, the two crossings marked by purple arrows remain unchanged away from the high symmetry path and are also parts of line nodes. For clarity, we mark the positions of the Weyl points by red and blue dots in Fig. 5a. Both are located around K and at about -30 meV below the Fermi energy, in contrast to the DFT-predicted Weyl points above the Fermi energy, which evolve into line nodes in our calculations. Similar gap closure and the presence of nodes near the Fermi energy are also found in Mn_3Ge , as pointed out by colored arrows in Fig. 4c.

To understand the origin of this evolution, we compare the band maps of Mn_3Sn on the $k_z = 0$ plane for $J = 0.6$ and 0.55 eV. For $J = 0.6$ eV shown in Fig. 5e, two bands cross at 9 meV along K-M-K (red line) but become gapped slightly off this path (blue line). They correspond to the Weyl points around K in DFT calculations and exist here for J beyond 0.6 eV. As J decreases, the top of the β band and the bottom of the α band are renormalized towards the Fermi energy, and their dispersions start to deviate from linearity near the nodes. For $J = 0.55$ eV, these nodes are pushed to about 50 meV but remain unaffected under a slight shift from the high symmetry path, so they are no longer Weyl points (Fig. 5f). In the meanwhile, the bands around K point at -0.1 eV that bend down at $J = 0.6$ eV are lifted towards the Fermi energy and renormalized to bend upwards at $J = 0.55$ eV. They eventually intersect with the β and γ bands around K and produce the Weyl points below the Fermi energy in Fig. 5c. Thus, these Weyl points start to show up only below $J \approx 0.6$ eV and move closer to the Fermi energy as J further decreases. They are not present in DFT calculations as shown in Supplementary Fig. S1. Their sensitive dependence on the Hund's rule coupling may be attributed to the rapid change of the Mn spin moment as J exceeds its critical value J_c , which in

turn changes the band dispersion as well as the relative band shift of different spin components (Supplementary Fig. S2). The sensitive tuning with the Hund's rule coupling implies that the Weyl nodes in Mn_3X systems are accidental and not protected by symmetry²².

Discussion

To summarize, we have performed systematic electronic band structure calculations of the inverse triangular antiferromagnets Mn_3X ($X = \text{Sn}, \text{Ge}$) using DFT+DMFT and found very different results compared to previous DFT calculations. The Hund's rule coupling is seen to play a key role for the magnetic, electronic, and topological properties. It determines the local spin state of Mn-ions, consequently the triangular AFM order, and the relative shift of the bands. A proper choice of the Hund's rule coupling can yield excellent agreement with the ARPES data in many details, which is not possible in previous DFT calculations even with an artificial band renormalization. In particular, the Mn- d electrons are found to be weakly correlated in both compounds, with a much smaller renormalization factor than previously estimated in Mn_3Sn .

The different band structures may have an influence on experimental interpretations. So far, direct experimental evidences are still lacking for the exact locations of the Weyl points, so that previous analyses were mostly based on DFT band structures, which may need to be reconsidered. For example, it has been argued that increasing Mn content may introduce more d electrons, shift the Fermi energy upwards to the DFT Weyl points, and hence enhance the anomalous Hall conductivity and longitudinal magnetoconductance¹³. However, as shown in Supplementary Fig. S4 for our self-consistent DFT+DMFT calculations of $\text{Mn}_{3+\delta}\text{Sn}_{1-\delta}$ with more Mn- d electrons, the band contacts above the Fermi energy around M point are located at around 8.2 meV in $\text{Mn}_{3.03}\text{Sn}_{2.97}$ and 7.4 meV in $\text{Mn}_{3.06}\text{Sn}_{0.94}$, which move less than 1 meV towards the Fermi energy and cannot account for the 60% reduction of the longitudinal magnetoconductance. It is therefore important to reexamine all previous experimental interpretations based on incorrect DFT band structures for an improved understanding of the topological properties and their experimental tuning. In addition, our results predict that the Weyl nodes in Mn_3X family systems may be sensitively tuned by controlling the size of the spin moment, possibly also by pressure^{32,42}.

Very recently, the Ga-rich Mn_3Ga was reported to have the highest Néel temperature and largest AHE in the Mn_3X compounds⁴³. The DFT seems to yield correct order of magnitude of the AHE, but its predicted monotonic increase with Mn vacancy was not observed in experiments. A unified explanation of the exotic properties in the whole Mn_3X family is desired based on correlated electronic structure calculations with a proper treatment of the Hund's rule coupling.

Methods

DFT calculations

The first-principles DFT calculations were performed by using the full-potential linearized augmented plane-wave method implemented in the WIEN2k package²³. The Muffin-tin radii (R_{MT}) were set to 2.5 a.u. for Mn and Sn, and the cutoff parameter of the basis was chosen such that $R_{MT}K_{\max} = 8.5$. We took 10000 \mathbf{k} -points in the whole Brillouin zone and used the generalized-gradient approximation with the Perdew-Burke-Ernzerhof (GGA-PBE) exchange-correlation potential⁴⁴.

DFT+DMFT calculations

Non-spin-polarized DFT calculations with SOC were first performed using the full potential code WIEN2k²³. Cluster DMFT calculations were then carried out for the noncollinear AFM order of Mn_3Sn and Mn_3Ge , but only the onsite self-energies were considered to avoid the negative sign problem as performed in Ref.⁴⁵. The directions of the spin polarization of local orbitals on each Mn-ion were fixed according to experimental observation illustrated in Fig. 1a. The magnitudes of the spin moments were determined self-consistently and found to differ slightly on inequivalent Mn-ions. Only their averages are shown in the figure for simplicity. Both the Hubbard U and the Hund's rule coupling J were added to all five Mn-3 d orbitals. The hybridization expansion continuous-time quantum Monte Carlo method (CTQMC) was chosen as the DMFT impurity solver⁴⁶, and the spectral functions were obtained using the maximum entropy method for analytic continuation of the self-energies⁴⁷.

Acknowledgements

We thank Satoru Nakatsuji, Kenta Kuroda, and Takeshi Kondo for generously sharing their ARPES data. This work was supported by the National Key Research and Development Program of China (Grant No. 2022YFA1402203), the National Natural Science Foundation of China (NSFC Grant No. 11974397), and the Strategic Priority Research Program of the Chinese Academy of Sciences (Grant No. XDB33010100).

References

- [1] Dzero, M., Xia, J., Galitski, V. & Coleman, P. Topological Kondo Insulators. *Annu. Rev. Condens. Matter Phys.* **7**, 249 (2016).
- [2] Chen, L. et al. Topological semimetal driven by strong correlations and crystalline symmetry. *Nat. Phys.* **18**, 1341-1346 (2022).
- [3] Brown, P. J., Nunez, V., Tasset, F., Forsyth, J. B. & Radhakrishna, P. Determination of the magnetic structure of Mn_3Sn using generalized neutron polarization analysis. *J. Phys.: Condens. Matter* **2**, 9409-9422 (1990).
- [4] Nakatsuji, S., Kiyohara, N. & Higo, T. Large anomalous Hall effect in a non-collinear antiferromagnet at room

- temperature. *Nature* **527**, 212-215 (2015).
- [5] Suzuki, M.-T., Koretsune, T., Ochi, M. & Arita, R. Cluster multipole theory for anomalous Hall effect in antiferromagnets. *Phys. Rev. B* **95**, 094406 (2017).
- [6] Li, X. et al. Anomalous Nernst and Righi-Leduc effects in Mn_3Sn : Berry curvature and entropy flow. *Phys. Rev. Lett.* **119**, 056601 (2017).
- [7] Higo, T. et al. Large magneto-optical Kerr effect and imaging of magnetic octupole domains in an antiferromagnetic metal. *Nat. Photon.* **12**, 73-78 (2018).
- [8] Kübler, J. & Felser, C. Non-collinear antiferromagnets and the anomalous Hall effect. *EPL* **108**, 67001 (2014).
- [9] Yang, H. et al. Topological Weyl semimetals in the chiral antiferromagnetic materials Mn_3Ge and Mn_3Sn . *New J. Phys.* **19**, 015008 (2017).
- [10] Kübler, J. & Felser, C. Weyl fermions in antiferromagnetic Mn_3Sn and Mn_3Ge . *EPL* **120**, 47002 (2017).
- [11] Fang, Z. et al. The anomalous Hall effect and magnetic monopoles in momentum space. *Science* **302**, 92-95 (2003).
- [12] Ma, J.-Z. et al. Observation of a singular Weyl point surrounded by charged nodal walls in PtGa. *Nat. Commun.* **12**, 3994 (2021).
- [13] Kuroda, K. et al. Evidence for magnetic Weyl fermions in a correlated metal. *Nat. Mater.* **16**, 1090-1095 (2017).
- [14] Cao, Y. & Yang, Y.-F. Flat bands promoted by Hund's rule coupling in the candidate double-layer high-temperature superconductor $\text{La}_3\text{Ni}_2\text{O}_7$ under high pressure. *Phys. Rev. B* **109**, L081105 (2024).
- [15] Mravlje, J. et al. Coherence-incoherence crossover and the mass-renormalization puzzles in Sr_2RuO_4 . *Phys. Rev. Lett.* **106**, 096401 (2011).
- [16] Georges, A., Medici, L. de' & Mravlje, J. Strong Correlations from Hund's Coupling. *Annu. Rev. Condens. Matter Phys.* **4**, 137-178 (2013).
- [17] Nayak, A. K. et al. Large anomalous Hall effect driven by a nonvanishing Berry curvature in the noncollinear antiferromagnet Mn_3Ge . *Sci. Adv.* **2**, e1501870 (2016).
- [18] Kiyohara, N., Tomita, T. & Nakatsuji, S. Giant anomalous Hall effect in the chiral antiferromagnet Mn_3Ge . *Phys. Rev. Appl.* **5**, 064009 (2016).
- [19] Wuttke, C. et al. Berry curvature unravelled by the anomalous Nernst effect in Mn_3Ge . *Phys. Rev. B* **100**, 085111 (2019).
- [20] Wu, M. et al. Magneto-optical Kerr effect in a non-collinear antiferromagnet Mn_3Ge . *Appl. Phys. Lett.* **116**, 132408 (2020).
- [21] Changdar, S. et al. Weak electronic correlations observed in magnetic Weyl semimetal Mn_3Ge . Preprint at <https://doi.org/10.48550/arXiv.2312.00511> (2023).
- [22] Xu, Y. et al. High-throughput calculations of magnetic topological materials. *Nature* **586**, 702-707 (2020).
- [23] Blaha, P., Schwarz, K., Madsen, G. K. H., Kvasnicka, D. & Luitz, J. Wien2k: An Augmented Plane Wave plus Local orbital Program for Calculating the Crystal Properties (Technical University of Wien in Austria, ISBN39501031-1-2) (2001).
- [24] Georges, A., Kotliar, G., Krauth, W. & Rozenberg, M. J. Dynamical mean-field theory of strongly correlated fermion systems and the limit of infinite dimensions. *Rev. Mod. Phys.* **68**, 13-125 (1996).
- [25] Anisimov, V. I., Poteryaev, A. I., Korotin, M. A., Anokhin, A. O. & Kotliar, G. First-principles calculations of the electronic structure and spectra of strongly correlated systems: dynamical mean-field theory. *J. Phys.: Condens. Matter* **9**, 7359-7367 (1997).
- [26] Lichtenstein, A. I. & Katsnelson, M. I. Ab initio calculations of quasiparticle band structure in correlated systems: LDA++ approach. *Phys. Rev. B* **57**, 6884-6895 (1998).
- [27] Kotliar, G. et al. Electronic structure calculations with dynamical mean-field theory. *Rev. Mod. Phys.* **78**, 865-951 (2006).
- [28] Held, K., Andersen, O. K., Feldbacher, M., Yamasaki, A. & Yang, Y.-F. Bandstructure meets many-body theory: the LDA+DMFT method. *J. Phys.: Condens. Matter* **20**, 064202 (2008).
- [29] Haule, K., Yee, C.-H. & Kim, K. Dynamical mean-field theory within the full-potential methods: Electronic structure of CeIrIn_5 , CeCoIn_5 , and CeRhIn_5 . *Phys. Rev. B* **81**, 195107 (2010).
- [30] Momma, K. & Izumi, F. VESTA 3 for three-dimensional visualization of crystal, volumetric and morphology data. *J. Appl. Cryst.* **44**, 1272-1276 (2011).
- [31] Romaka, L. et al. Peculiarity of component interaction in Zr-Mn-{Sn, Sb} ternary systems. *J. Alloy. Compd.* **611**, 401-409 (2014).
- [32] Sukhanov, A. S. et al. Gradual pressure-induced change in the magnetic structure of the noncollinear antiferromagnet Mn_3Ge . *Phys. Rev. B* **97**, 214402 (2018).
- [33] Soh, J.-R. et al. Ground-state magnetic structure of Mn_3Ge . *Phys. Rev. B* **101**, 140411 (2020).
- [34] Sung, N. H., Ronning, F., Thompson, J. D. & Bauer, E. D. Magnetic phase dependence of the anomalous Hall effect in Mn_3Sn single crystals. *Appl. Phys. Lett.* **112**, 132406 (2018).
- [35] Tomiyoshi, S. & Yamaguchi, Y. Magnetic structure and weak ferromagnetism of Mn_3Sn studied by polarized neutron diffraction. *J. Phys. Soc. Jpn.* **51**, 2478-2486 (1982).
- [36] Chen, X. et al. Unconventional Hund metal in a weak itinerant ferromagnet. *Nat. Commun.* **11**, 3076 (2020).
- [37] Li, M. et al. Dirac cone, flat band and saddle point in kagome magnet YMn_6Sn_6 . *Nat. Commun.* **12**, 3129 (2021).
- [38] Yu, T. et al. Correlated electronic structure of the kagome metal Mn_3Sn . *Phys. Rev. B* **106**, 205103 (2022).
- [39] Shim, J. H., Haule, K. & Kotliar, G. Fluctuating valence in a correlated solid and the anomalous properties of δ -plutonium. *Nature* **446**, 513-516 (2007).
- [40] Ikhlas, M. et al. Large anomalous Nernst effect at room temperature in a chiral antiferromagnet. *Nat. Phys.* **13**, 1085-1090 (2017).
- [41] Chen, T. et al. Anomalous transport due to Weyl fermions in the chiral antiferromagnets Mn_3X , $\text{X} = \text{Sn}, \text{Ge}$. *Nat. Commun.* **12**, 572 (2021).
- [42] Reis, R. D. dos et al. Pressure tuning of the anomalous Hall effect in the chiral antiferromagnet Mn_3Ge . *Phys. Rev. Mater.* **4**, 051401(R) (2020).
- [43] Song, L. et al. Large anomalous Hall effect at room temperature in a Fermi-level-tuned kagome antiferromagnet. *Adv. Funct. Mater.*, 2316588 (2024).
- [44] Perdew, J. P., Burke, K. & Ernzerhof, M. Generalized gradient approximation made simple. *Phys. Rev. Lett.* **77**, 3865 (1996).
- [45] Xu, Y., Sheng, Y. & Yang, Y.-F. Mechanism of the insulator-to-metal transition and superconductivity in the spin liquid candidate NaYbSe_2 under pressure. *npj Quantum Mater.* **7**, 21 (2022).

- [46] Haule, K. Quantum Monte Carlo impurity solver for cluster dynamical mean-field theory and electronic structure calculations with adjustable cluster base. *Phys. Rev. B* **75**, 155113 (2007).
- [47] Jarrell, M. & Gubernatis, J. E. Bayesian inference and the analytic continuation of imaginary-time quantum Monte Carlo data. *Phys. Rep.* **269**, 133-195 (1996).

Hundness and band renormalization in the kagome antiferromagnets Mn_3X

Yingying Cao,^{1,2} Yuanji Xu,³ and Yi-feng Yang^{1,2,4,*}

¹Beijing National Laboratory for Condensed Matter Physics and Institute of Physics, Chinese Academy of Sciences, Beijing 100190, China

²School of Physical Sciences, University of Chinese Academy of Sciences, Beijing 100049, China

³Institute for Applied Physics, University of Science and Technology Beijing, Beijing 100083, China

⁴Songshan Lake Materials Laboratory, Dongguan, Guangdong 523808, China

Here we give more analyses of DFT and DFT+DMFT calculations and their comparisons with ARPES in Mn_3Sn .

A. Comparison of DFT and ARPES

Figure S1 compares the ARPES data¹ and the DFT band structures without (a-d) and with (e-h left) artificial renormalization for the AFM1 configuration calculated using the noncollinear magnetic version of the WIEN2k package². As shown in Fig. S1a and the right part of Fig. S1e, above the Fermi energy the DFT bands without renormalization seem at first glance to match well with experiment along the high symmetry path Γ -K-M, but actually the band top around K is located at different energies, about -0.2 eV in DFT and -0.04 eV in ARPES. The right parts of Figs. S1f and S1g show the ARPES bands along the k_x direction away from the high symmetry path by a small shift Δk_y . The electron pockets around K vanish while that around M remains till $\Delta k_y = -0.144(2\pi/a)$, which is very different in DFT (Figs. S1b and S1c) where those around K first vanish at $\Delta k_y = -0.072(2\pi/a)$ but reappear at $\Delta k_y = -0.144(2\pi/a)$ and

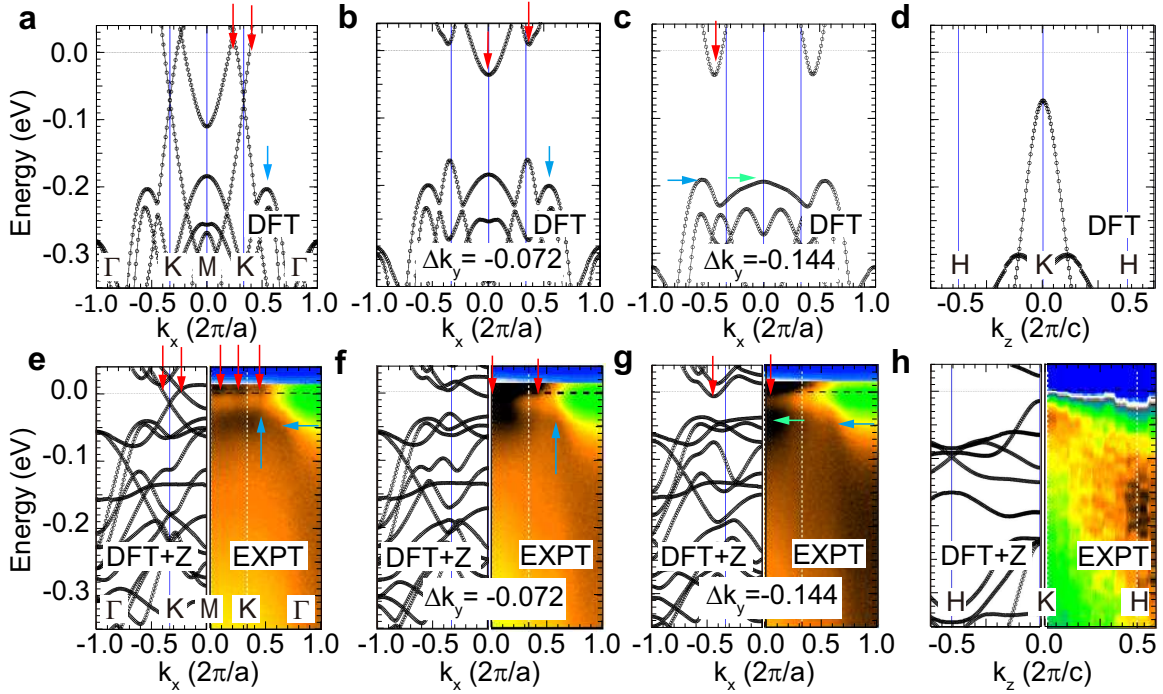


FIG. S1: Comparison of DFT and ARPES (EXPT) band structures along several paths in the Brillouin zone. **a,e** The high symmetry path Γ -K-M-K- Γ ; **b,f** The k_x direction away from the high symmetry path by $\Delta k_y = -0.072(2\pi/a)$; **c,g** The k_x direction away from the high symmetry path by $\Delta k_y = -0.144(2\pi/a)$; **d,h** The high symmetry path H-K-H. **a-d** show the DFT band structures without renormalization, and **e-h** compare the renormalized DFT band structures (left) and the ARPES data (right)¹.

*yifeng@iphy.ac.cn

the one around M disappears at $\Delta k_y = -0.144(2\pi/a)$. In addition, there exist obvious spectral weights around -0.2 eV near H in experiment (right part of Fig. S1h) but nothing is seen in DFT (Fig. S1d).

Figures S1e-S1h compare the ARPES data (right) and the DFT band structures renormalized by a factor of 5 (left). Now the bands near the Fermi energy along the K-M path and H seem to agree better, but there are still obvious inconsistencies. First, the renormalization introduces a lot of spectral weights along the K-M cut between -0.3 and -0.1 eV, which are not present in experiment (Fig. S1e). Second, the position of the electron pocket still differs at $\Delta k_y = -0.144(2\pi/a)$ away from the high symmetry path Γ -K-M as shown in Fig. S1g.

B. DFT+DMFT band structures with varying U and J

Figure S2 shows the DFT+DMFT spectral functions on a high symmetry path at 300 K for different values of U and J . As J increases from 0.53 (a), 0.55 (e), 0.6 (b) to 0.7 eV (c) for a fixed $U = 6$ eV, the bands enclosed in the red box move downwards and the M-shaped band enclosed in the orange box moves up. Such a relative shift of different bands is also seen along A- Γ as marked by the green arrows. Similar changes are present in Figs. S2d-S2f

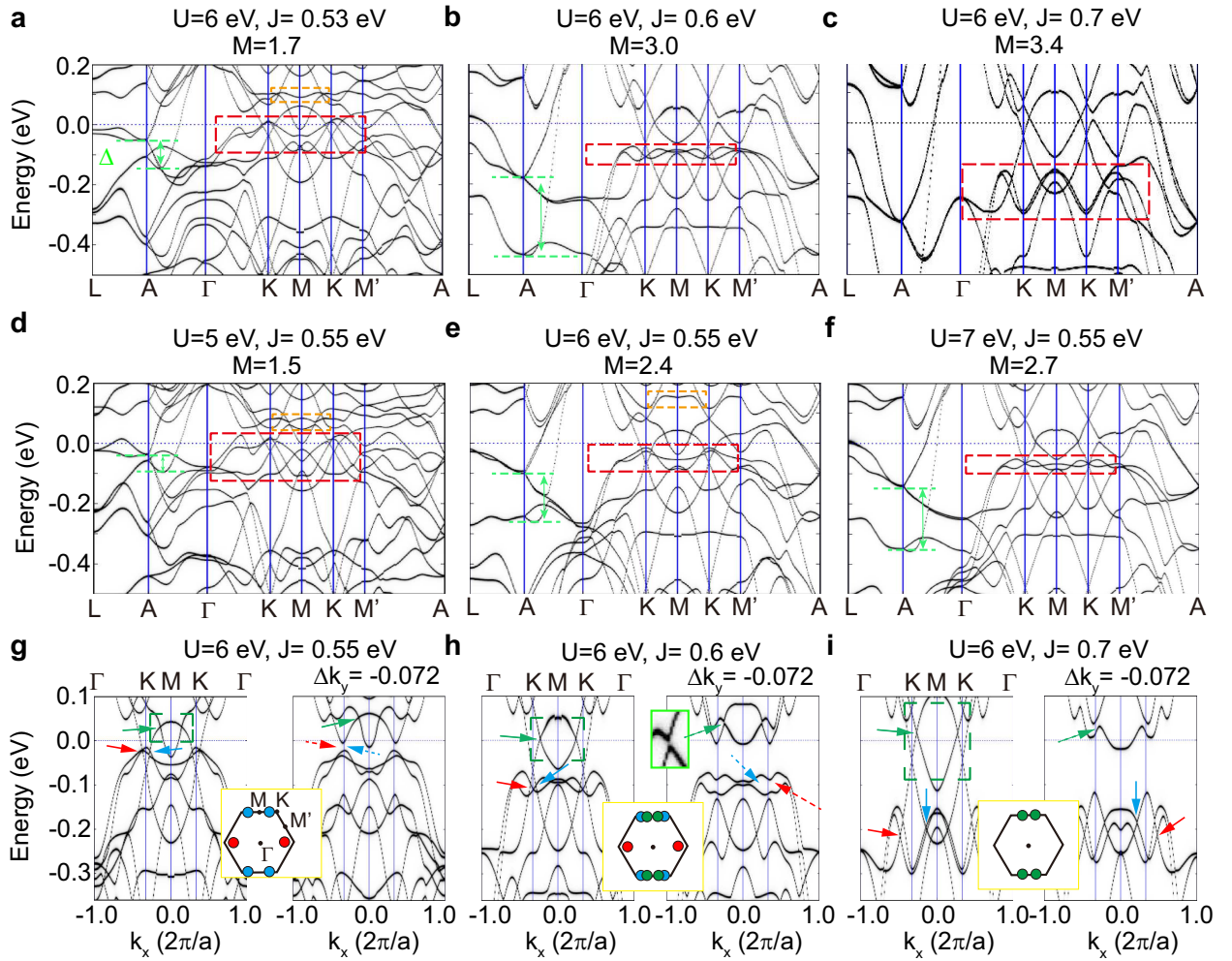


FIG. S2: Evolution of the DFT+DMFT spectral functions with varying J and U at 300 K. For clarity, the imaginary part of the self-energy is set to zero to reduce the band broadening. The calculated Mn spin moment is also given for comparison. **a-c** show the band evolution with varying J for a fixed $U = 6$ eV and **d-f** show the evolution with U for a fixed $J = 0.55$ eV. The green lines and arrows define the relative shift Δ between two featured energy bands. The red boxes show the band crossings below the Fermi energy. The orange boxes highlight the M-shaped band above the Fermi energy. **g-i** show the evolution of the Weyl points in the DFT+DMFT band structures with varying J at $U = 6$ eV. The green boxes show the band crossings above the Fermi energy. The insets show the positions of the Weyl points in the Brillouin zone, as indicated by the arrows of the same color in the spectral function plots. The solid arrows indicate the band crossings and the dashed ones indicate the gaps.

with increasing U for a fixed J . A straightforward comparison indicates that the relative band shift Δ is tuned by the size of the spin moment M . In the meanwhile, the bands in the red box get narrowed close to the critical Hund's rule coupling J_c , indicating a stronger renormalization near J_c as discussed in Fig. 2d and causing the flat bands below the Fermi energy along the K-M path observed in ARPES¹.

Thus, the sensitive dependency of the DFT+DMFT band structures on the Hund's rule coupling arises from the rapid variation of the spin moment M above the critical J_c . We have shown in the main text that the results at $J = 0.55$ eV for $U = 6$ eV agree well with the ARPES. A slightly larger J can already yield some inconsistency. As shown in Fig. S2b for $J = 0.6$ eV, the flat bands enclosed in the red box along K-M-K is located at about -0.1 eV rather than -0.04 eV as reported in ARPES¹.

More analyses are given in Figs. S2g-S2i with varying J at $U = 6$ eV and $T = 300$ K. The green boxes mark the band crossings formed by one hole band and one electron band. As J increases, the hole band moves upwards and the electron band moves downwards, but the energy of the crossing points remains almost unchanged. They correspond to the Weyl points in DFT. However, away from the high symmetry path M-K by a small shift $\Delta k_y = -0.072$ ($2\pi/a$), the crossings remain for $J = 0.55$ eV but open a gap for $J = 0.6$ and 0.7 eV (green arrows) in our DFT+DMFT calculations, indicating that they are not Weyl points at $J = 0.55$ eV. On the other hand, the band crossings inside the red boxes move downwards away from the Fermi energy with increasing J . At $J = 0.55$ and 0.6 eV, they open a clear gap for $\Delta k_y = -0.072$ ($2\pi/a$) and form the Weyl points at around -30 meV around K (red and blue arrows) as discussed in the main text. But for $J = 0.7$ eV, they are no longer Weyl points. We thus conclude that the DFT Weyl points only exist above the Fermi energy for large J and evolves into line nodes below $J = 0.6$ eV, while the DFT+DMFT Weyl points appear below the Fermi energy below around $J = 0.6$ eV and move towards the Fermi energy with decreasing J .

C. Effect of a small net magnetization

Figure S3 compares the DFT+DMFT band structures of AFM1 configuration in Mn_3Sn and those with a small net magnetization of $13 \text{ m}\mu_{\text{B}}/\text{uc}$ obtained by rotating all Mn moments towards a axis according to the magnetization experiment reported in Ref.¹. We find that neither the line nodes above the Fermi energy nor the Weyl points below the Fermi energy are affected. Such a small tilting of the spin moments is a negligible perturbation to the electronic topology and thus ignored for simplicity.

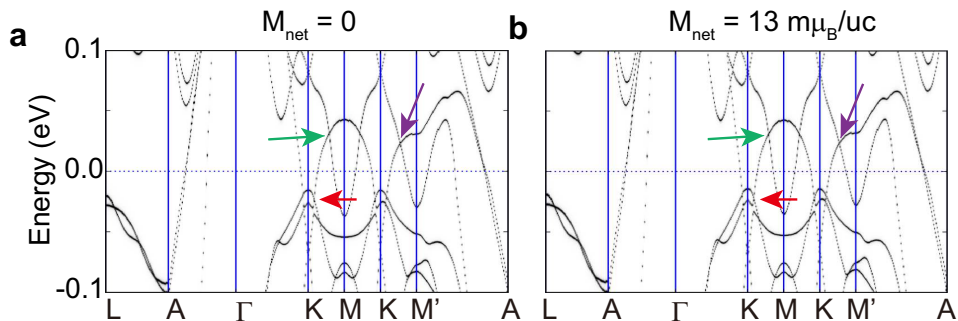


FIG. S3: **Comparison of the DFT+DMFT spectral functions for AFM1 configuration without and with a small net magnetization.** The imaginary part of the self-energy is set to zero for a better view of the band structures. The parameters are $U = 6$ eV, $J = 0.55$ eV, and $T = 300$ K. The net moment is set to $13 \text{ m}\mu_{\text{B}}/\text{uc}$ in **b** as observed in experiment¹.

D. Effect of electron doping

Figure S4 shows the DFT+DMFT band structures for different Mn and Sn compositions. An upshift of the Fermi energy of about 10 meV is enough to resemble the electron doping in $\text{Mn}_{3.06}\text{Sn}_{0.94}$, while in DFT it requires an upshift of 40 meV¹. The position of the nodes marked by green arrows change only slightly from 8.2 meV in $\text{Mn}_{3.03}\text{Sn}_{0.97}$ to 7.4 meV in $\text{Mn}_{3.06}\text{Sn}_{0.94}$. This small energy shift less than 1 meV differs from previous expectations. On the other hand, the Weyl point marked by red arrows is pushed to -37 meV, slightly further away from the Fermi energy, and the node marked by purple arrows moves downwards slightly to touch the Fermi energy, which may be important for explaining the anomalous Nernst effect observed in experiment³.

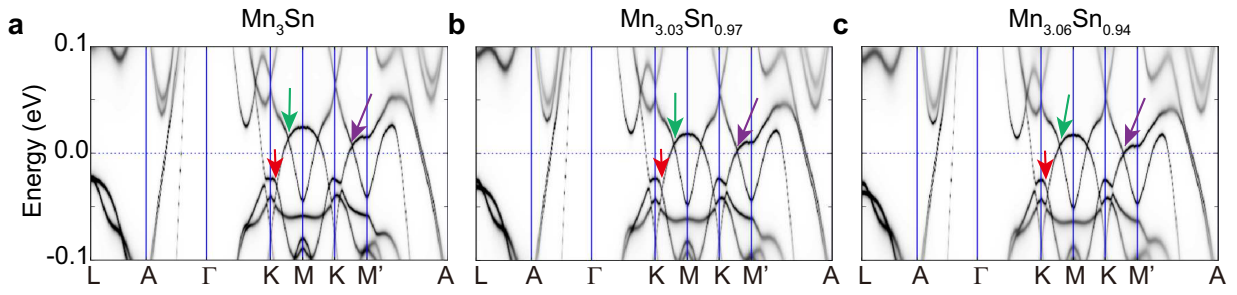


FIG. S4: Evolution of the DFT+DMFT spectral functions with varying Mn and Sn compositions. The parameters are $U = 6$ eV, $J = 0.55$ eV, and $T = 60$ K.

References

- [1] Kuroda, K. et al. Evidence for magnetic Weyl fermions in a correlated metal. *Nat. Mater.* **16**, 1090-1095 (2017).
- [2] Laskowski, R., Madsen, G. K. H., Blaha, P. & Schwarz, K. Magnetic structure and electric-field gradients of uranium dioxide: An *ab initio* study. *Phys. Rev. B* **69**, 140408(R) (2004).
- [3] Ikhlas, M. et al. Large anomalous Nernst effect at room temperature in a chiral antiferromagnet. *Nat. Phys.* **13**, 1085-1090 (2017).